A Monolithic Forward-View Optical Scanner by a Pair of Upright MEMS Mirrors on a SiOB for LiDAR Applications

Dingkang Wang, Dong Zheng, Sanjeev J. Koppal, *Senior Member, IEEE*, Boqian Sun, and Huikai Xie, *Fellow, IEEE*

***Abstract*— A forward-view optical scanner made of a MEMS mirror typically needs a second mirror to fold the optical beam forward, and thus an assembly structure is required, which drastically increases the overall size and weight of the scanner. This paper reports an ultra-small forward-view optical scanner with two vertically oriented micromirrors integrated on a silicon optical bench (SiOB). A new latch structure is proposed to secure the mirror frame at its vertical position and an array of meander thin-film stripes is designed to assist the latching process. The new design has been successfully fabricated and shows much-improved verticality with a maximum deviation of less than ±2° from 90°. With an optical aperture of 0.7 mm, the form factor of the MEMS chip is 4.9 mm (length) by 4.7 mm (width) by 1.8 mm (height). The measured forward field of view (FoV) of the vertical micromirrors reaches 21° in both axes at non-resonance with the voltage amplitude less than 4 V. The first resonant frequency (corresponding to the mirror frame rotation mode) of the micromirror is about 630 Hz. A fiber-pigtail bonded forward scanner is assembled with a footprint of 2 cm by 1.2 cm and a weight of 0.6 g. A forward scanning LiDAR has been built with this new MEMS scanner. The non-resonant scanning capability enables forward-view adaptive resolution and zoom-in scanning capability. [2021-0132]**

***Index Terms*— MEMS mirror, LiDAR, electrothermal actuation, forward-scanning.**

I. Introduction

LIGHT detection and ranging (LiDAR) has garnered significant interest as a ranging technology because it can achieve true distance measurement and does not rely on ambient light. Meanwhile, microrobots are also demanding the capability of LiDAR [1]. However, conventional LiDAR systems are bulky and usually employ motorized scanners that are large and have weights in the order of kg's, and they have limited scanning rate, reliability issues, and high cost [2]. Thus, miniaturizing LiDAR systems, especially their optical scanners, is needed.

Microelectromechanical system (MEMS) technology is widely used to miniaturize various electromechanical and optical systems. MEMS mirrors, due to their small size [3]–[5], fast response [6]–[8], and good reliability under several conditions [4], [9], [10], have been exploited to build compact LiDAR systems. MEMS mirrors also have some unique advantages over traditional motorized scanning LiDAR, such as adaptive FoV, adaptive resolution, arbitrary scanning patterns, and zoom-in scanning capability [11]. Both electrostatic and electromagnetic MEMS mirrors have been incorporated into LiDAR systems [3], [4], [12]. For example, Mitsubishi reported a LiDAR system based on a dual-axis MEMS mirror with an overall LiDAR size of 108 mm × 96 mm × 95 mm [4]. Kasturi *et al.* demonstrated a LiDAR-based on an electrostatic MEMS mirror with a size of 90 mm × 60 mm × 40 mm and a weight of 46 g [3]. The Intel L515 MEMS-based LiDAR has a small size of 61 mm × 61 mm × 26 mm [12]. The fast axis scanning of these MEMS mirrors typically works at resonance, requiring additional optical angular detection and control. Also, electrostatic MEMS mirrors need large space for their comb drives while electromagnetic MEMS mirrors require large coils or magnets to generate the actuation force, so their fill factors are typically low (mostly less than 5%) [13]. In contrast, electrothermal bimorph-based MEMS mirrors have large fill factors (∼20%) due to their gimbal-less structural design [14]. For example, Jia *et al.* developed a 2-axis electrothermal MEMS mirror with a fill factor of 25% using an inverted-series-connected (ISC) electrothermal bimorph actuator design [5]. Using this ISC actuator design, Wang *et al.* developed an electrothermal MEMS mirror-based multi-functional LiDAR with the dimensions of 210 mm × 90 mm × 65 mm [12]. In addition, the electrothermally actuated MEMS mirror also have a wide operational temperature range [10], which makes it suitable for LiDAR under several working conditions. Unfortunately, the weights and dimensions of micro-air vehicles (MAVs) are typically below 100 g and 100 mm, respectively [15], [16]. Thus,

Manuscript received June 20, 2021; revised July 20, 2021; accepted July 21, 2021. This work was supported in part by the US Office of Naval Research under Award #N00014-18-1-2663 and in part by the National Science Foundation (NSF) Multi-functional Integrated System Technology (MIST) Center at the University of Florida. Subject Editor N. Quack. *(Corresponding author: Huikai Xie.)*

Dingkang Wang, Dong Zheng, and Sanjeev J. Koppal are with the Department of Electrical and Computer Engineering, University of Florida, Gainesville, FL 32611 USA (e-mail: noplaxochia@ufl.edu).

Boqian Sun is with the School of Information and Electronics, Beijing Institute of Technology, Beijing 100811, China.

Huikai Xie is with the School of Information and Electronics, Beijing Institute of Technology, Beijing 100811, China, and the BIT Chongqing Center of Microelectronics and Microsystems, Chongqing 400030, China (e-mail: hkxie@ieee.org).

Color versions of one or more figures in this article are available at https://doi.org/10.1109/JMEMS.2021.3100077.

Digital Object Identifier 10.1109/JMEMS.2021.3100077

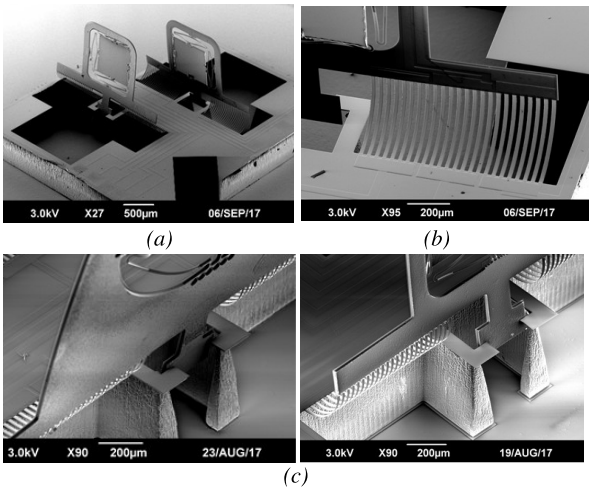

Fig. 1. Previous design [18]. (a) A SEM of the device. (b) An arrays of bending bimorph beams. (c) The SEMs of the stoppers in the previous works with large vertical bending variations.

those MEMS-based LiDAR are still significantly oversized and overweighed for MAVs.

Besides, forward-view detection is critical for all MAVs. Thus, assembling an extra mirror to fold the laser beam is needed to scan forward, which drastically increases the overall size and weight. For instance, Wang *et al.* developed a compact forward-viewing LiDAR prototype based on an electrothermal MEMS mirror and an additional fixed mirror to fold the laser beam, but the overall dimensions after being packaged with the additional mirror were increased to 100 mm × 100 mm × 60 mm [17]. Several groups have all use two scanning MEMS mirrors to relay the optical beam for forward-view scanning. However, the dimensions of those scanning modules are still 100-200 mm and weigh 5 g to 20 g, which are one to two orders of magnitude larger and heavier than single MEMS mirrors.

To eliminate the extra folding mirror, the authors proposed and demonstrated a monolithic forward-view MEMS laser scanner with two vertical micromirrors integrated on one silicon optical bench (SiOB), which weighed only 20 mg [18]. This novel design (see Fig. 1(a)) significantly reduces the packaging size and assembling and alignment efforts. However, the vertical orientation angles of the MEMS mirrors had large deviations in the range of $-27°$ to $+10°$ from exactly 90° (see Fig. 1(c)) [18], which not only brings uncertainties to the forward scanning direction but also needs extra efforts or structures to adjust the scanning direction. Furthermore, the vertical micromirrors were held out of the plane by arrays of bending bimorph beams (see Fig. 1(b)). So, the mirror frames were not secured, significantly affecting the 2D scanning of the vertical micromirrors.

Therefore, in this work, a new latch structure, as illustrated in Fig. 2(b), is proposed to lock and secure the mirror frame at 90°. This latch structure replaces the previous stopper structure on the SiOB and can lock the vertical position after the mirror frame is released. Also, to guide the mirror frame into the latch, a group of thin-film stripes is designed on the mirror frame as an assistance structure. The new SiOB based MEMS vertical micromirrors is successfully fabricated and exhibit much better verticality, much less coupling from the mirror frame, and improved stiffness. A preliminary demonstration was reported in [14]. More details in the structural design and device characterization of this MEMS mirror are given in this paper. Furthermore, a forward scanning LiDAR system based on this novel monolithic dual-mirror MEMS mirror has been built and LiDAR point clouds with zoom-in scanning and adaptive resolution scanning have been successfully generated.

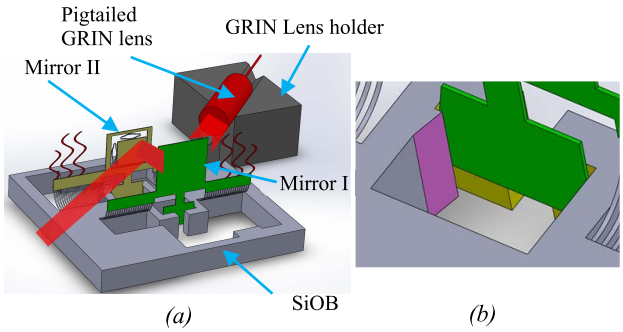

Fig. 2. (a) A 3D model of the MEMS scanner with two vertical mirrors on a SiOB with a pigtailed GRIN lens on a lens holder. (b) The new latch structure design.

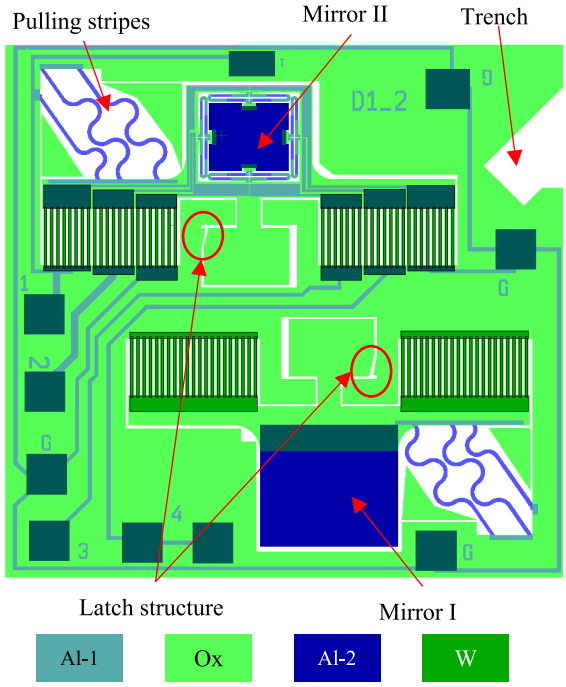

Fig. 3. The proposed device topology with the latch structure and the pulling strings.

II. Device Design

A. Topology Design

As illustrated in Fig. 2(a), the two vertically oriented micromirrors (Mirror I and Mirror II) are both designed to stand upright on the SiOB. The alignment trench on the SiOB can assist the alignment of the laser beam. The laser beam first reaches Mirror I. Then Mirror II folds the laser beam and scans the laser in the forward direction.

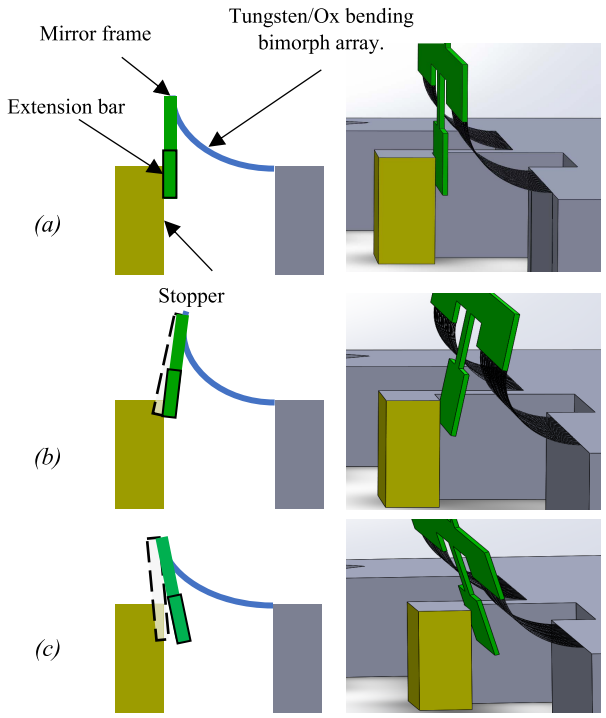

Fig. 4. The problems of the previous stopper. (a) Ideal case. (b) If the W/SiO_2 beams are over-stressed, the tilt of the mirror frame will be larger than 90°. (c) If the W/SiO_2 beams are under-stressed, the tilt of the mirror frame will be smaller than 90°.

Mirror I can be a non-scanning fixed mirror or a scanning mirror, while Mirror II is always a 2-axis scanning micromirror. Fig. 3 shows the layout of such a dual-vertical mirror design, where Mirror I is a fixed mirror with a reflective area of 1.2 mm by 1.1 mm while Mirror II is a 2-axis scanning mirror with a mirror plate of 0.7 mm by 0.6 mm. In the case where both the two mirrors are configured as scanning mirrors since the aperture of Mirror II is 1.4 mm by 1.2 mm, much larger than that of Mirror I, the laser beam will not be truncated even when Mirror I scans its full range. A trench on the silicon substrate is aligned 45° to Mirror I for laser alignment. Mirror II is also parallel to Mirror I along the designed optical path. The distance between the two mirrors is only 1.2 mm. The bar extended from the bottom of the mirror frame is expected to fit into the latch structure at an exact vertical position. There are pulling stripes that are attached to the mirror frame and can be cut off from the other end on the silicon substrate.

The vertical scanning mirrors are electrothermally-actuated and based on the inverted-series-connected (ISC) bimorph actuation structure reported in [5]. The MEMS mirror has a footprint of 4.9 mm by 4.7 mm. Mirror I and Mirror II are bent by 42 and 44 W/SiO_2 bending bimorph beams, respectively.

B. Latch Structure Design

Like the previous design, the vertical bending is achieved through highly stressed Tungsten (W)/SiO_2 bimorph arrays [18]. In the previous design [18], a stopper structure together with an extension bar is implemented, as illustrated in Fig. 4(a), in which ideally the stopper and the bar can stop

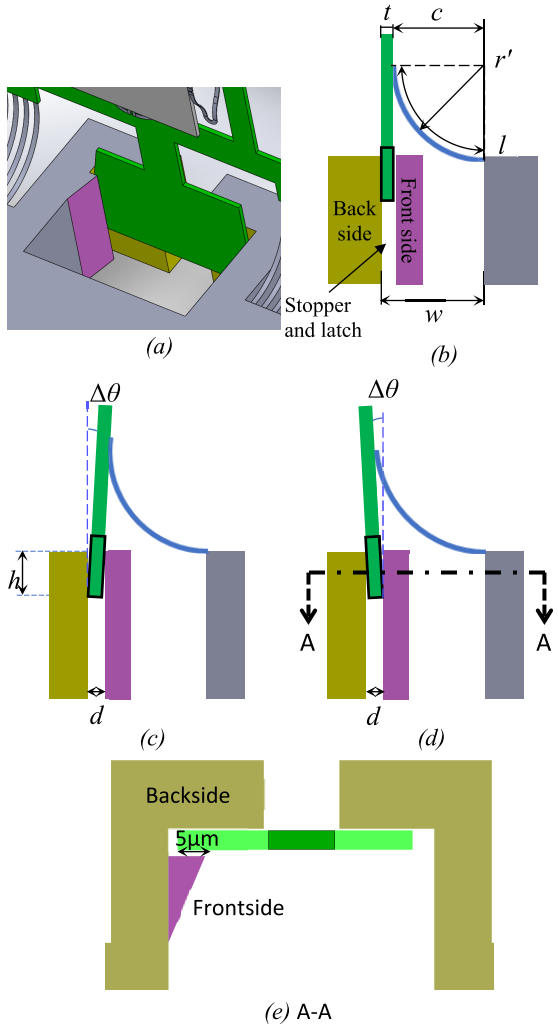

Fig. 5. (a) The latch design. (b) The expected result of the latch structure. The lower bounds (c) and upper bound (d) of the vertical mirror frame with the latch structure. (e) The cross-section view of the latch structure. (Draws are not to scale.)

the mirror frame at exactly 90°. However, fabrication variations always cause nonideal results. Due to the non-uniform deposition nature of the tungsten sputtering process and the variance of the chamber condition from one wafer to another, the embedded stress of the sputtered tungsten varies. Another issue is that the silicon sidewalls are not so straight, typically sloped with an undercut angle around 80°, due to the use of a non-optimized DRIE recipe. Thus, the mirror frame will always be tilted even when the W/SiO_2 beams are over-stressed, as shown. When the W/SiO_2 beams are under-stressed, the tilt of the mirror frame may be quite large, as in the cases in Fig. 4(c) and Fig. 4(b). Since the electrical current for generating the electrothermal actuation goes through the W layer of the W/SiO_2 beams, Joule heating is also induced in the W/SiO_2 beams and thus causes its radius of curvature of the W/SiO_2 bimorph array to change, which creates another scanning variation issue.

To overcome all the deficiencies of the previous stopper design, a new latch design is proposed and illustrated in Fig. 5(a). The mirror frame bar will fall into the latch

structure, and the bending angle of the mirror frame will be fixed at 90°, as illustrated in Fig. 5(b).

The latch structure requires the bar of the mirror frame fits into the notch on the silicon substrate. The designed width of the notch is wider than the thickness of the mirror frame ($t = 20\ \mu$m) to make sure the mirror frame bar can always fit into the notch. The front side of the latch side-wall is 5 μm longer than the end of the mirror frame bar to make sure the latch can work, as shown in Fig. 5(e).

To reach the target bending angle θ, the length, l, of the W/SiO_2 bimorphs follow:

$$l = r\theta \tag{1}$$

where r is the radius of curvature of the bending bimorph. The latch structure requires that the bending bimorph array always bends the mirror frame to an angle θ equal to or larger than 90°. Increasing the stress level in the W layer can decrease r and thus decrease l, but too much stress in the W layer will cause it to peel off. Increasing the length of the bimorph beams can increase the bending angle without increasing the stress level, despite decreasing the bimorph stiffness. Experiments show that the average radius of curvature, r, of the W/SiO_2 bimorphs is 273 μm with a standard deviation of 34 μm. Thus, to ensure $\theta \geq 90°$ with a high confidence level of 95%, the length of the bending mirror frame is selected to be $l =$ 470 μm.

Next, we need to figure out the position of the latch structure. The latch structure has two sides. As the MEMS mirror frame will be corrected down to 90°, the releasing force will make the mirror frame bar contact with the backside of the latch. Ignore the thickness of the bending bimorph (~1.5 μm), the position of the backside of the latch measured from the Si substrate is,

$$w = r + t \tag{2}$$

where t is the thickness of the mirror frame, r is the radius of the corrected bending bimorphs.

$$r = \frac{l}{\theta} = \frac{470\ \mu\text{m}}{\pi/2} \approx 300\mu\text{m} \tag{3}$$

So, the position of the backside of the latch is $w = 320\ \mu$m.

The gap of the latch notch d is determined by the thickness of the mirror frame and the tolerance of the vertical bending angle. The gap between the two sides d should be larger than the thickness of the mirror frame to allow the bar of the mirror frame to get into the notch, so $d > 20\ \mu$m. The tolerance of the vertical bending angle is $\Delta\theta = 1.5°$. So, the value of d is,

$$d = 2\tan(\Delta\theta)\, h + t = 38\ \mu\text{m} \tag{4}$$

where $h = 340\ \mu$m is the length of the part of the mirror frame bar inside the notch.

C. Pulling Stripes Design

Fitting the mirror frame bar into the notch is still challenging. There is a good chance that the bar of the mirror frame gets stuck at the slope of the front side of the latch due to friction. Thus, assistant pulling strings are added to the mirror frame, as shown in the layout in Fig. 3. The pulling stripes have two functions. First, they can help to slow down the unwanted silicon etching of the backside of the mirror plate during release to ensure the stiffness and flatness of the mirror plate. Second, the pulling stripes can be used as an acting point to guide the mirror frame and fit the frame bar into the notch if the bar does not fall into the notch automatically. The layer structure of the pulling strings is a stack of 0.2 μm Pt, 1.1 μm Al and 1 μm SiO_2 to make sure they will not break easily during the release or being pulled.

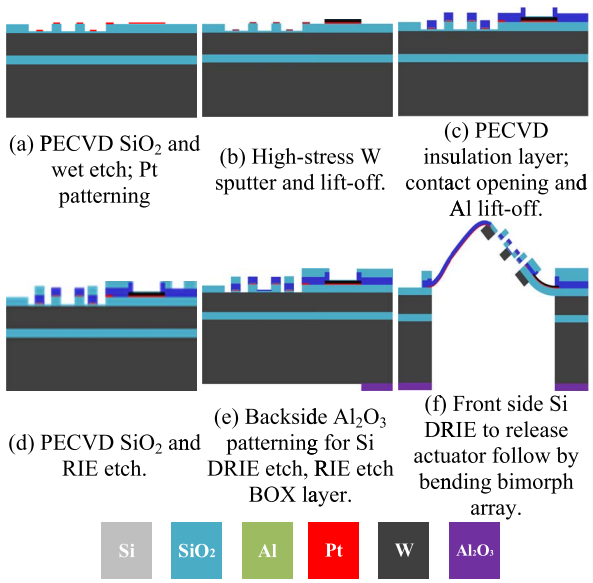

Fig. 6. The fabrication process flow until the mirror frame is released from the wafer.

III. Fabrication and Release

The device is fabricated with an SOI wafer whose device layer is 20 μm thick, which defines the thicknesses of the mirror plates and the vertical mirror frames. The SOI handle layer thickness is 500 μm. The process flow is illustrated in Fig. 6. In the first step (Fig. 6(a)), a 1 μm-thick SiO_2 layer is deposited on the device layer via plasma-enhanced chemical vapor deposition (PECVD) followed by photolithography and wet etching to form the bottom layer of the bimorph actuators. Next, as shown in Fig. 6(b), a 0.2 μm-thick Pt layer is sputtered to form the heater layer for the bimorph actuators and the first layer of the pulling stripes. Then a 0.49 μm-thick tungsten (W) layer is sputtered and patterned. During the W sputtering, the Ar pressure is carefully tuned and maintained at 6.5 mTorr to produce W films with a high tensile stress of about 1 GPa. After that, a 1.1 μm-thick Al layer is sputtered to form the bimorph actuators and another layer of the pulling stripes. Then a 1.1 μm SiO_2 layer and a thin Al reflective layer are consecutively patterned for the bimorph actuators and as the mirror reflective surface, respectively (Fig. 6(d)). On the backside, a 200 nm-thick Al_2O_3 layer is patterned as the DRIE etching mask. The DRIE etching of the handle-layer silicon is closely monitored, and the etching/passivation times are tuned during the etching to make sure the verticality of the notch. Finally, an anisotropic DRIE on the front side will etch through the device layer to expose the sidewalls of the silicon underneath the bimorphs and the pulling stripes, and then an

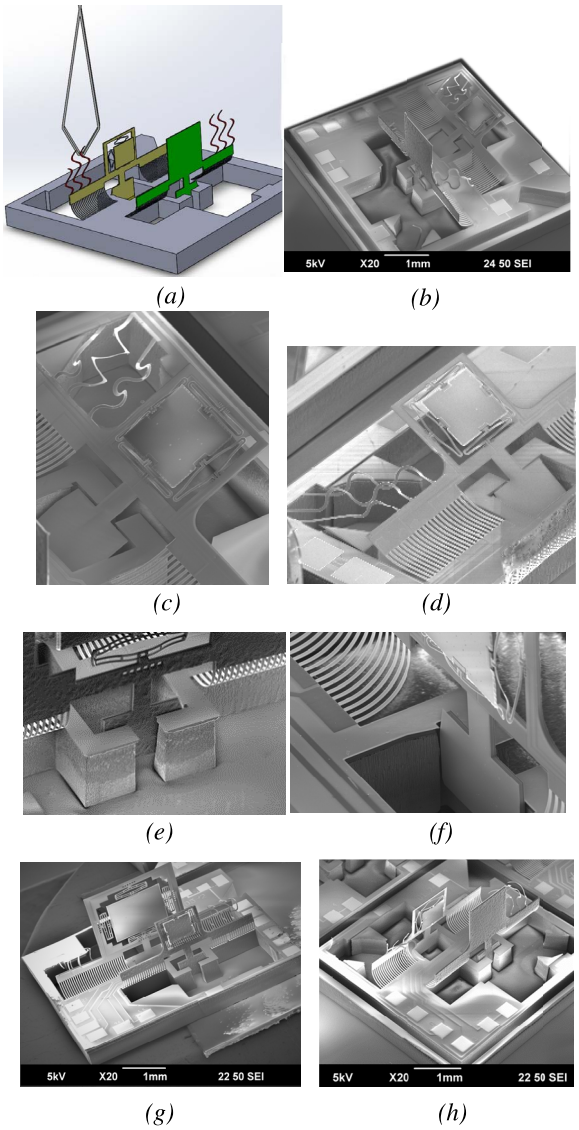

Fig. 7. (a) Pull the stripes to guide the mirror frame bar into the latch. (b) A released device is with the pulling strings for Mirror I cut and those for Mirror II remaining. SEMs of fabricated devices after released and with the mirror frame bar guided into the stop-and-latch. (c, d) Zoom-in images of the mirror frame bar before the stripes are cut. (e, f) Zoom-in images of the mirror frame bar inside the latch structure after the stripes are cut. (g) A forward scanner with two scanning mirrors of different sizes. (h) The forward scanner with a scanning mirror and a fixed mirror.

isotropic etching is done to undercut the silicon to release the bimorphs including the bimorph actuators, the vertical bending bimorph arrays, and the pulling stripes. The residual stresses in the thin films of the bimorphs result in initial out-of-plane displacements of the mirror plates (Fig. 6(f)). However, due to the presence of the pulling stripes, the mirror frame will stay at around 40° bending positions.

Fig. 7(b) shows the fabricated device after the DRIE release step. On the SiOB, the pulling stripes on Mirror II hold the mirror frame so the mirror frame is balanced at around 40°, as shown in Fig. 7(c, d). The backside of the mirror frame is in contact with the front side of the latch. This can prevent excessive mirror backside etching during DRIE isotropic etch. The pulling stripes of Mirror II are easily cut with a sharp tweezer. The success rate is relatively high (∼80%). The strength of the pulling stripes is higher than we expected. In the future design, only one stripe is sufficient to keep the mirror frame at the position. In that case, we can design an electrical fuse in the stripe and use a pulse of current to burn and break the stripe. Using fewer stripes and arrange the stripes further away from the scanning mirror also eliminates the issue that the floating stipes may impede the light transmission.

The stress of the W/SiO_2 bimorph array will bend the mirror frame towards 90°. The mirror frame is supposed to fall into the latch structure and secure itself. If the mirror frame does not fall into the latch, then the tweezer can be used to manually pull the pulling stripes and guide the mirror frame to fall into the latch without touching the mirror frame structure, as shown in Fig. 7(a). Fig. 7(e, f) shows the detail of the latch structure after the stripes are cut, where the lower part of the mirror frame bar is inside the latch. The figures also show that the undercuts of the latch sidewalls are from 89° to 91° thanks to the better control of the DRIE backside etching process, which is a significant improvement from the previous batch of devices. The full view of two slightly different devices is shown in Fig. 7 (g, h).

TABLE I

THE STATISTICS OF THE BENDING ANGLE OF THE DEVICES FROM PREVIOUS WORKS AND THIS WORK

	No. of devices	Min.	Max.	Std. Dev.	Absolute Error (AE) to 90°
Previous devices	21	63.4°	99.3°	10.5°	9.5 °
This work	12	90.0°	95.8°	2.0°	2.3°

IV. DEVICE CHARACTERIZATION

A. MEMS Mirror Verticality

To evaluate the benefit of the new latch structure, the bending angles of 12 vertical mirrors from this work and 21 vertical micromirrors from the previous works [18] with the simple stopper structure are measured with a microscope (OLYMPUS BX51) and a measurement stage (QUADRA-CHEK 200). The bending angle is the angle of a mirror frame measured from its initial flat position. The statistical results are listed in Table I. The orientation angles of the 12 new vertical micromirrors range from 90.0° to 95.8° with a standard deviation of 2.0°, which are much improved from the range of 63.4° to 99.3° with a standard deviation of 10.5° of the previous designs. Fig. 8 compares the distribution of the mirror frame angles from this work and the previous works in the violin plot. The devices made from this works show better control of the mirror frame's vertical bending angle.

B. Quasi-Static Response and Frequency Response

The measured non-resonant scanning angles of a vertical micromirror (Mirror I) are plotted in Fig. 9(a), where their

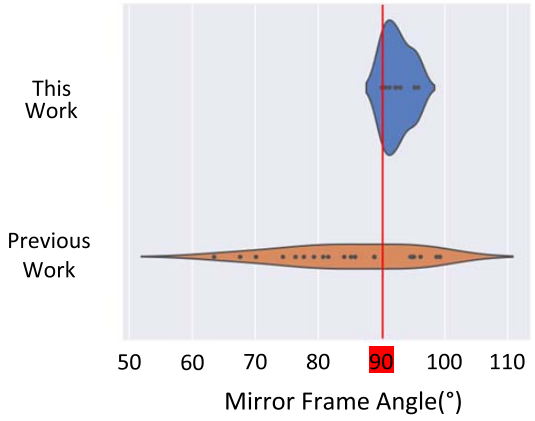

Fig. 8. A comparison between the sample distribution of the measured mirror frame angles from this work and the previous works.

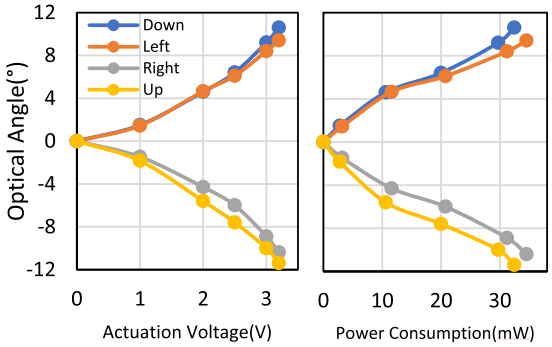

(a)

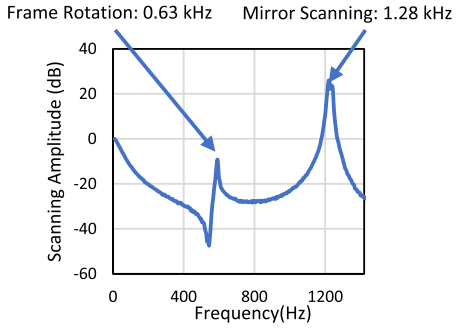

(b)

Fig. 9. (a) The quasi-static optical scanning angle response of the MEMS mirror to voltage and power. (b) The frequency response of the MEMS mirror and mirror frame.

maximum optical scanning FoVs are 20° (h) × 22° (v). The measured frequency response is shown in Fig. 9(b). The −3dB scanning bandwidth is 50 Hz. The first mode is the mirror frame rotation mode at 0.63 kHz, improved from 0.38 kHz of the previous design due to the adoption of the new latch structure. The second mode is the tip-tilt scanning mode at 1.28 kHz.

C. Mirror Frame Rotation

The frame rotation is an unwanted response during the mirror actuation. The bending bimorph array conducts the electrical current to the vertical micromirror and thus draws Joule heating that tends to cause the mirror frame to rotate upward. With the new latch structure in place, the mirror frame bar is latched inside the notch, so the rotation of the mirror frame is constrained. As shown in Table II, the maximum frame rotation angle of this new design is reduced to 0.05° from 0.58° of the previous design.

TABLE II
THE COMPARISON OF THE FRAME ROTATION AND THE RESONANT FREQUENCY OF THE FRAME ROTATION MODE

	Maximum frame rotation during mirror actuation	The resonant frequency of the frame rotation mode
This work	0.05°	0.63 kHz
Previous work	0.58°	0.38 kHz

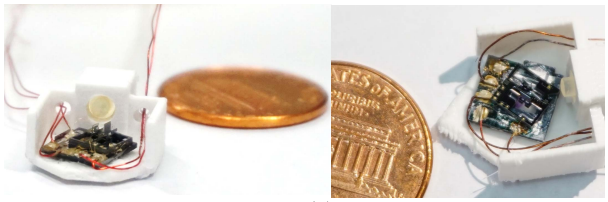

(a)

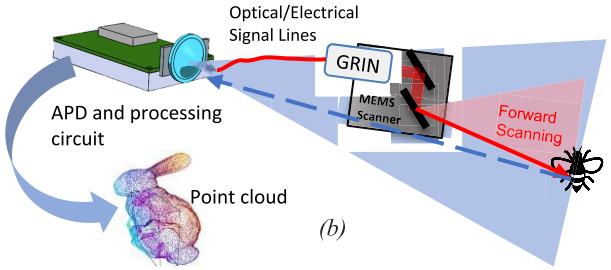

(b)

Fig. 10. (a) A miniaturized forward scanning MEMS scanner. (b) The schematic of the forward view LiDAR.

V. MEMS LiDAR Demonstration

A. MEMS LiDAR System

A compact and lightweight forward-view scanning head for LiDAR scanning is built with this device, as shown in Fig. 10(a). The MEMS device is assembled in a 3D printed holder with a size of 20 mm by 12 mm by 7 mm and a weight of 0.6 g. The laser is delivered through a single-mode fiber and a GRIN lens. A GRIN lens with an outer diameter of 1.8 mm and a laser beam size of 1 mm. Since the laser beam size is larger than the MEMS mirror plate, a portion of the laser power will be lost. There exists a divergence angle of the laser beam and the radius of curvature of the mirror plate will further increase the divergence angle. This leads to an overall angular resolution of 12 mrad. The incident laser direction is visually aligned with the alignment trench on the SiOB. In the future, a holder with higher precision will be made for automatically aligning the laser with the MEMS mirrors. Wire bonding and soldered wires are used to deliver the control signals to the scanning mirror.

A LiDAR system (Fig. 10(b)) is built to assess the performance of the forward-view scanner. We adopted a LiDAR architecture first reported in [19]. This LiDAR has two parts.

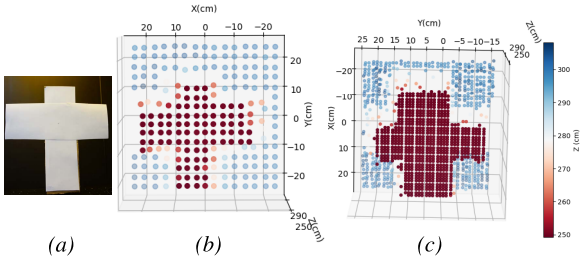

Fig. 11. (a) The Target object. (b) With the MEMS mirror scanning at 10 Hz (h) × 0.5 Hz (v), a point cloud with 20 by 20 pixels is generated. (c) With the MEMS mirror scanning at 5 Hz (h) × 0.125 Hz (v), a point cloud with 40 by 40 pixels is generated.

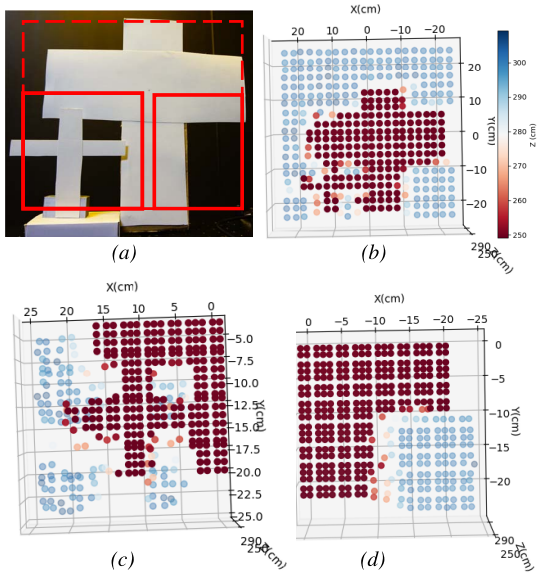

Fig. 12. The demonstration of forward view zoom-in scanning capability. (a) The target objects. Without changing scanning frequency, the MEMS scanning FoV is set to (b) ±4.5° in both axes, (c) 4.5°∼0° (h) by −4.5°∼0° (v), and (d) 0.5°∼4.5° (h) by −4.5°∼0° (v).

The MEMS forward-view scanner head is expected to be carried by a moving MAV and emit a scanning laser in pulses, while all other components, like the laser source, the photodetector, and the signal processing units are all on the ground as the LiDAR base. The LiDAR base may be fixed on a bench, or it may be on a ground robot that can follow the MAV in a distance. The MEMS scanning angle, the motion of the robots, and the time-of-flight (ToF) are processed to generate the point cloud.

The laser source is a gain-switch fiber laser (Leishen, LEP-1550-600) with a pulse width of 15 ns, a center wavelength of 1550 nm, and a peak power of 40 W. The MEMS mirror is actuated by the PWM signals from an Arduino Uno. The scanning angle is controlled through a look-up-table method. The photodetector is an InGaAs avalanche photodetector (Thorlabs, APD130C). The return signal is sent to a comparator and the ToF is measured by a time-to-digital converter (Texas Instruments, TDC7201). The Arduino collects the ToF data and sends it together with the MEMS scanning angle information to a computer to reconstruct the point clouds. The LiDAR can acquire 400 ToF data points per second and detect a maximum range of 4 m. The LiDAR receiver can detect the return laser pulse longer than 4 m but the measurement suffers from low SNR and poor spatial resolution due to the divergence of the laser beam.

B. MEMS LiDAR Experiments

The MEMS scanning capability and the LiDAR point cloud results are demonstrated in this section. Fig. 11 shows the adaptive resolution scanning capability. Fig. 11(a) is a target placed 2.4 m away from the LiDAR, and the background is 0.6 m behind the target. The MEMS mirror scans a FoV of ±4.5° in both axes and the scanning frequencies can be controlled in a wide range. The MEMS scanning frequency is adjusted to 10 Hz (h) × 0.5 Hz(v) and 5 Hz (h) × 0.125 Hz (v), and the point cloud in each frame are 20 by 20 pixels and 40 by 40 pixels, as shown in Fig. 11(b) and (c), respectively. As the MEMS mirror scans at lower frequencies, more detail of the target can be recovered in the point cloud.

Fig. 12 shows the zoom-in scanning capability of the forward-view MEMS-based LiDAR. Two paper crosses (Fig. 12(a)) were used as the target. Fig. 12(b) shows a full FoV (±4.5°) of the target. The MEMS mirror was actuated at 10 Hz (h) × 0.5 Hz (v), so the LiDAR generated 20 by 20 points per frame. In Fig. 12(c) and (d), the MEMS mirror scanning FoV was set to −4.5°∼0° (h) by −4.5°∼0° (v) and 0.5°∼4.5° (h) by −4.5°∼0° (v), respectively, with the same frequencies. As the MEMS mirror zooms in into a certain region of the object, more details of the features of the target can be visualized and without sacrificing the frame rate.

VI. Conclusion

In this work, a forward-view MEMS scanner with a latch structure to improve the verticality of the upright micromirrors is designed and fabricated. Compared to the previous designs, the latch structure can latch the mirror frame to secure the bending angles of both vertical micromirrors. The pulling stripes are also designed on the mirror frame so that we can drag the pulling stripes to direct the mirror frame into the latch structure. With the new latch structure, the forward-view scanner design shows much-improved verticality in both static and dynamic scanning states. The error of the mirror frames' vertical bending angle decreases from 9.5° to 2.3°. The stiffness is also improved by 1.7 times, making the micromirrors more robust. A forward-view scanning MEMS LiDAR has been built with this MEMS scanner with a footprint of 20 mm by 12 mm and a weight of 0.6 g. The acquired point clouds yield a maximum range of 4 m and a 2-axis FoV of 9° by 9°. This new LiDAR configuration enables forward-view adaptive point cloud density ranging and zoom-in scanning, which has potential applications in MAVs and micro-robots.

References

[1] C. Sampedro *et al.*, "A fully-autonomous aerial robotic solution for the 2016 international micro air vehicle competition," in *Proc. Int. Conf. Unmanned Aircr. Syst. (ICUAS)*, Jun. 2017, pp. 989–998.

[2] R. Halterman and M. Bruch, "Velodyne HDL-64E LiDAR for unmanned surface vehicle obstacle detection," *Proc. SPIE*, vol. 7692, May 2010, Art. no. 76920D.

[3] A. Kasturi, V. Milanovic, B. H. Atwood, and J.Yang, "UAV-borne LiDAR with MEMS mirror-based scanning capability," *Proc. SPIE*, vol. 9832, May 2016, Art. no. 98320M.

[4] Mitsubishi Electric. (May 18, 2021). *Mitsubishi Electric Develops MEMS LiDAR Solution for Autonomous Vehicles*. [Online]. Available: https://www.mitsubishielectric.com/news/2020/0312.html
[5] K. Jia, S. Pal, and H. Xie, "An electrothermal tip–tilt–piston micromirror based on folded dual S-shaped bimorphs," *J. Microelectromech. Syst.*, vol. 18, no. 5, pp. 1004–1015, Oct. 2009.
[6] L. Ye, G. Zhang, and Z. You, "Large-aperture kHz operating frequency Ti-alloy based optical micro scanning mirror for LiDAR application," *Micromachines*, vol. 8, no. 4, p. 120, Apr. 2017.
[7] S. Gu-Stoppel *et al.*, "A highly linear piezoelectric quasi-static MEMS mirror with mechanical tilt angles of larger than 10," *Proc. SPIE*, vol. 10931, Mar. 2019, Art. no. 1093102.
[8] U. Hofmann *et al.*, "Resonant biaxial 7-mm MEMS mirror for omni-directional scanning," *J. Micro/Nanolithogr., MEMS, MOEMS*, vol. 13, no. 1, Dec. 2013, Art. no. 011103.
[9] Y. Hua, S. Wang, B. Li, G. Bai, and P. Zhang, "Dynamic modeling and anti-disturbing control of an electromagnetic MEMS torsional micromirror considering external vibrations in vehicular LiDAR," *Micromachines*, vol. 12, no. 1, p. 69, Jan. 2021.
[10] P. Wang, Y. Liu, D. Wang, H. Liu, W. Liu, and H. Xie, "Stability study of an electrothermally-actuated MEMS mirror with Al/SiO_2 bimorphs," *Micromachines*, vol. 10, no. 10, p. 693, Oct. 2019.
[11] Z. Tasneem, D. Wang, H. Xie, and K. Sanjeev, "Directionally controlled time-of-flight ranging for mobile sensing platforms," in *Proc. Robot., Sci. Syst. (RSS)*, Jun. 2018.
[12] F. Lourenço and H. Araujo, "Intel RealSense SR305, D415 and L515: Experimental evaluation and comparison of depth estimation," in *Proc. 16th Int. Joint Conf. Comput. Vis., Imag. Comput. Graph. Theory Appl.*, 2021, pp. 362–369.
[13] V. Milanović, A. Kasturi, J. Yang, and F. Hu, "Closed-loop control of gimbal-less MEMS mirrors for increased bandwidth in LiDAR applications," *Proc. SPIE*, vol. 10191, May 2017, Art. no. 101910N.
[14] X. Zhang, L. Zhou, and H. Xie, "A fast, large-stroke electrothermal MEMS mirror based on Cu/W bimorph," *Micromachines*, vol. 6, no. 12, pp. 1876–1889, 2015.
[15] H. V. Phan, T. Kang, and H. C. Park, "Design and stable flight of a 21 g insect-like tailless flapping wing micro air vehicle with angular rates feedback control," *Bioinspiration Biomimetics*, vol. 12, no. 3, Apr. 2017, Art. no. 036006.
[16] A. T. Baisch and R. J. Wood, "Design and fabrication of the Harvard ambulatory micro-robot," in *Robotics Research*. Berlin, Germany: Springer, 2011, pp. 715–730.
[17] D. Wang, L. Thomas, S. Koppal, Y. Ding, and H. Xie, "A low-voltage, low-current, digital-driven MEMS mirror for low-power LiDAR," *IEEE Sensors Lett.*, vol. 4, no. 8, pp. 1–4, Aug. 2020.
[18] D. Wang, C. Watkins, S. Koppal, and H. Xie, "A silicon optical bench with vertically-oriented micromirrors for active beam steering," *Sens. Actuators A, Phys.*, vol. 298, Oct. 2019, Art. no. 111586.
[19] D. Wang, H. Xie, L. Thomas, and S. Koppal, "A miniature LiDAR with a detached MEMS scanner for micro-robotics," *IEEE Sensors J.*, early access, May 12, 2021, doi: 10.1109/JSEN.2021.3079426.

Dingkang Wang received the B.E. degree in mechanical engineering and electrical engineering Jilin University China in 2016 and the Ph.D. degree in mechanical engineering and electrical engineering from University of Florida in 2021. His research interests include microelectromechanical (MEMS) systems, micro/nano fabrication, and light detection and ranging (LiDAR) systems.

Dong Zheng received the B.S. degree in automation from Northeast University in 2010 and the M.E. degree in electrical engineering from the Stevens Institute of Technology in 2014. He is currently pursuing the Ph.D. degree with the Department of Electrical and Computer Engineering, University of Florida, Gainesville, FL, USA. His research interests include microelectromechanical (MEMS) systems, micro/nanofabrication, optical coherence tomography (OCT), and lung cancer.

Sanjeev J. Koppal (Senior Member, IEEE) received the B.S. degree from the University of Southern California in 2003 and the master's and Ph.D. degrees from the Robotics Institute, Carnegie Mellon University. After CMU, he was a Post-Doctoral Research Associate with the School of Engineering and Applied Sciences, Harvard University. Prior to joining UF, he was a Researcher with the Texas Instruments Imaging Research and Development Laboratory. He is currently an Associate Professor with the Department of Electrical and Computer Engineering, University of Florida. His interests span computer vision, computational photography and optics, novel cameras and sensors, 3D reconstruction, physics-based vision, and active illumination.

Boqian Sun received the B.S. degree in instrumentation science and technology from Xidian University and the Ph.D. degree in instrumentation science and technology from Tsinghua University, China. He is currently an Assistant Professor with the School of Information and Electronics, Beijing Institute of Technology, Beijing, China. His current research interest includes high-precision MEMS mirrors and sensors.

Huikai Xie (Fellow, IEEE) received the B.S. degree in microelectronics from Beijing Institute of Technology, the M.S. degree in photonics from Tufts University, and the Ph.D. degree in electrical and computer engineering from Carnegie Mellon University. He worked with the University of Florida as an Assistant Professor (2002–2007), an Associate Professor with tenure (2007–2011), and a Full Professor (2011–2020). He is currently a Professor with the School of Information and Electronics, Beijing Institute of Technology, Beijing, China. He has published over 300 technical papers, 11 book chapters, and holds over 30 US patents. His current research interests include MEMS/NEMS, optical beam steering, optical communications, LiDAR, NIR spectroscopy, and optical microendoscopy. He is a fellow of SPIE. He is also an Associate Editor of the IEEE SENSORS LETTERS and *Sensors and Actuators A: Physical*.